Geophysical Research Letters

RESEARCH LETTER
10.1029/2021GL093373

Cold Pools Observed by Uncrewed Surface Vehicles in the Central and Eastern Tropical Pacific

Samantha M. Wills[1,2], **Meghan F. Cronin**[2], **and Dongxiao Zhang**[1,2]

[1]Cooperative Institute for Climate, Ocean, and Ecosystem Studies, University of Washington, Seattle, WA, USA, [2]Pacific Marine Environmental Laboratory, NOAA, Seattle, WA, USA

Key Points:

- Saildrone uncrewed surface vehicles (USVs) observed atmospheric cold pools over observationally sparse regions of the central and eastern tropical Pacific
- In situ measurements reveal new insights on high-frequency variations in surface meteorological and oceanic variables associated with atmospheric cold pools
- USV clusters provide unique temporal and spatial vantage points for resolving smaller-scale phenomena over the ocean

Correspondence to:
S. M. Wills,
smwills@uw.edu

Citation:
Wills, S. M., Cronin, M. F., & Zhang, D. (2021). Cold pools observed by uncrewed surface vehicles in the central and eastern tropical Pacific. *Geophysical Research Letters*, *48*, e2021GL093373. https://doi.org/10.1029/2021GL093373

Received 15 MAR 2021
Accepted 1 MAY 2021

© 2021. The Authors.
This is an open access article under the terms of the Creative Commons Attribution-NonCommercial-NoDerivs License, which permits use and distribution in any medium, provided the original work is properly cited, the use is non-commercial and no modifications or adaptations are made.

Abstract New in situ observations collected by Saildrones, a novel uncrewed surface vehicle (USV), are used to investigate atmospheric cold pools during three 6-month missions to the central and eastern (~140°W–125°W) tropical Pacific. Cold pool fronts in the atmospheric boundary layer are identified by a −1.5°C air temperature drop occurring in 10 min or less. While cold pool events were observed in the central Pacific as far north as 30°N and within the equatorial band, the majority of observed cold pools occurred within the convective, low-wind shear environment of the Intertropical Convergence Zone. Composite time series analysis of measurements during the 382 cold pool events reveals new insights on high-frequency variations in air temperature, wind speed, humidity, pressure, and sea surface temperature and salinity associated with cold pool fronts. The results highlight the unique capabilities of Saildrone USVs to resolve small spatial and temporal scales of variability over observationally sparse ocean regions.

Plain Language Summary New, remotely piloted observing platforms have allowed us to observe atmospheric cold pools over hard-to-reach areas of the tropical oceans. Atmospheric cold pools form when rain evaporates under a thunderstorm, leading to the formation of a colder, denser air mass relative to the surrounding environment. Over the tropical oceans, atmospheric cold pools influence large changes in air temperature and wind speed, which are important for the exchange of heat between the ocean and the atmosphere. In this study, we evaluate oceanic and atmospheric data collected by these new, remotely piloted observing platforms to better understand the physical processes associated with atmospheric cold pools on smaller time and space scales over remote regions of the central and eastern tropical Pacific Ocean.

1. Introduction

Atmospheric cold pools generated over the tropical oceans are a key source of high-frequency variability in temperature, wind, and humidity near the air-sea interface. Over oceanic regions, atmospheric cold pools vary in size depending on the scale of parent convection but typically range between 10 and 200 km in diameter with lifespans on the order of hours to a day (Chandra et al., 2018; de Szoeke et al., 2017; Feng et al., 2015; Young et al., 1995). Cold pools occur when rainfall evaporates under precipitating clouds from convective and mesoscale systems, forming downdraft regions of relatively colder, unsaturated air that spread out horizontally upon reaching the surface (Betts & Silva Dias, 1979; Glickman & Zenk, 2000; Lafore & Moncrieff, 1989). Strong surface winds accompany the leading edge (i.e., the "gust front") that can displace ambient air through mechanical lifting and enhanced buoyancy from air-sea sensible and latent heat fluxes (Charba, 1974; Gentine et al., 2016; Langhans & Romps, 2015; Ross et al., 2004; Saxen & Rutledge, 1998; Tompkins, 2001). Previous studies have shown that cold pools are important for triggering convective updrafts along their outflow boundaries and organizing shallow and deep convection in low-wind shear environments over the tropical oceans (Emanuel et al., 1994; Garg et al., 2020; Li et al., 2014; Skyllingstad & de Szoeke, 2015; Torri et al., 2015; Zuidema et al., 2017).

Uncertainty surrounding the role of atmospheric cold pools in tropical convection remains, however, in large part due to the limited availability of high-resolution in situ observations over remote ocean regions to (1) validate findings from previous modeling experiments and satellite measurements and (2) resolve the finer spatial and temporal scales of variability associated with convective activity (Serra, 2018). In the central and eastern tropical Pacific, previous intensive observing periods to study subseasonal variability in deep convection and interactions with ocean processes have been limited to the far eastern Pacific (i.e.,

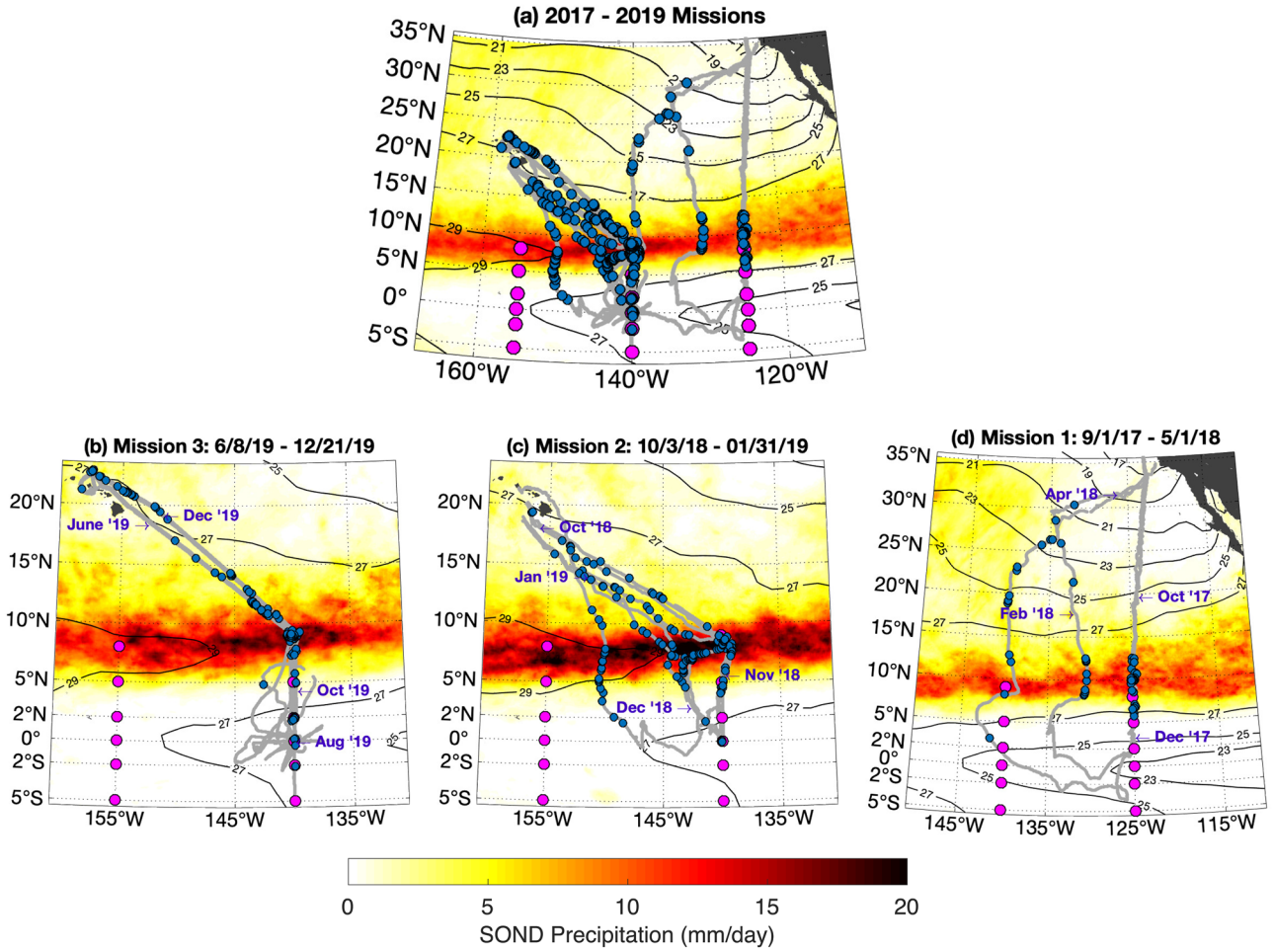

Figure 1. (a) Saildrone USV tracks (light gray contours) and locations of sampled cold pool events (blue dots) from the 2017, 2018, and 2019 Missions, collectively. Background shading and contours represent the climatological-mean September-December (SOND) precipitation rates (mm/day) and SST field (°C), respectively, for the 2017–2019 time period. TAO buoy locations are denoted by closed magenta circles. (b–d) Same as in (a), except for the individual (b) 2019, (c) 2018, and (d) 2017 Missions. The maps are zoomed in on the individual mission tracks, labeled with dates (purple text) to highlight the trajectories. Mean precipitation and SST are shown in each panel for the respective 2017, 2018, and 2019 SOND seasons.

95°W) during the Eastern Pacific Investigation of Climate Processes (EPIC) campaign in 2001 (Raymond et al., 2004), to ~8°N–10°N, 125°W during the Pan American Climate Studies (PACS) Tropical Eastern Pacific Process Study (TEPPS) in 1997 (Yuter & Houze, 2000) and the Salinity Processes in the Upper-ocean Regional Study (SPURS-2) in 2017 (Lindstrom et al., 2017). While these field campaigns covered a range of different boundary-layer environments throughout the region, an observational study of atmospheric cold pools has been lacking for the central and eastern tropical Pacific.

Fortunately, recent technological advancements in uncrewed surface vehicles (USVs) have allowed for new observations of tropical convection and atmospheric cold pools over remote, observationally sparse regions of the central and eastern tropical Pacific (~140°W–125°W). Saildrone USVs are autonomous wind- and solar-powered sailing drones, manufactured and piloted by Saildrone, Inc., that are seven meters in length, with a five meter tall wing, and capable of traveling far distances (~16,000 NM or ~30,000 km) for long durations of time (~12 months). The drones are outfitted with oceanic, atmospheric, and biogeochemical sensors that collect high-quality, high-resolution measurements at the air-sea interface (Zhang et al., 2019, cf. Figure 1). Saildrone sensor measurements have previously been validated through ship-saildrone-buoy comparisons that found good agreement across observing platforms (Zhang et al., 2019). All Saildrone USVs report realtime telemetered 1-min mean and standard deviation data to shore, and high-frequency delayed-mode data (i.e., 1 and 10 Hz) is stored on board for later recovery. Here, we present Saildrone data

collected during three 6-month missions to the central and eastern tropical Pacific that can resolve the rapidly evolving, small-scale processes associated with atmospheric cold pools over the ocean.

The overarching goal of this paper is to use these high spatial and temporal resolution surface meteorological observations from Saildrone USVs to quantify atmospheric variability associated with cold pool events in the central and eastern tropical Pacific. The results presented herein can be used as metrics for testing model products and demonstrate the utility of this novel technology for exploring and monitoring various scales of variability, particularly within the tropical Pacific. The remainder of this paper is organized as follows. Section 2 outlines the observational datasets and satellite products included in the present study, and Section 3 details the methodologies for calculating cold pool statistics and performing composite analysis. Section 4 presents a Saildrone case study and highlights composite time series results of cold pool events sampled by Saildrones USVs. A summary of key results is provided in Section 5.

2. Data

2.1. Saildrone Field Studies

Three Saildrone missions to the central and eastern tropical Pacific were completed as part of a pilot study for the Tropical Pacific Observing System (TPOS)-2020 project (Cravatte et al., 2016; Kessler et al., 2019). The first mission (September 1, 2017–May 1, 2018) had two Saildrone USVs that traversed from Alameda, CA at 38°N, 122°W to the SPURS-2 study region at 10°N, 125°W (Lindstrom et al., 2017) and then down to the equator at 125°W (Zhang et al., 2019) before returning to California. The second mission (October 3, 2018–January 31, 2019) had four Saildrone USVs that launched from Honolulu, HI at 21°N, 158°W to travel to the equator at 140°W, but the mission was cut short due to navigational difficulties in the low-wind, high ocean current regime of the Trade-wind forced equatorial Pacific. The third 6-month mission (June 8–December 21, 2019) involved four Saildrone USVs modified with improved navigation capability that launched again from Honolulu, HI to the equator at 140°W. Over the 3 years, the Saildrones covered a total distance of 74,000+ NM (or 137,000+ km) traveled, collecting measurements of wind speed, atmospheric temperature and humidity (AT/RH), air pressure, and sea surface temperature (SST) and salinity, respectively, at heights of 5, 2.4, 0.3, and −0.6 m above the water line. Due to the AT/RH and wind sensor sampling schemes on the Saildrones, 1-min mean AT/RH and wind speed and direction measurements were collected every 5 min in the 2017 and 2018 Missions, while the sampling schemes in the 2019 Mission were updated to collect measurements every minute. The realtime telemetered 1-min data for select variables from all three missions is publicly available through NOAA PMEL [https://www.pmel.noaa.gov/ocs/saildrone/data-access].

2.2. NDBC Tropical Atmosphere Ocean (TAO) Array

The Tropical Atmosphere Ocean (TAO) array maintained by NOAA's National Data Buoy Center (NDBC), is a network of moored buoys across the tropical Pacific ocean within 9° of the equator between 165°E and 95°W (McPhaden, Busalacchi, & Anderson, 2010; McPhaden, Busalacchi, & Cheney, et al., 1998). The buoys provide near-realtime and long-term historical records of in situ oceanic and atmospheric observations (https://www.pmel.noaa.gov/tao/drupal/disdel/). In this study, we obtain 10-min resolution data for the TAO buoy at 2°N, 140°W for comparison against Saildrone USV measurements during an atmospheric cold pool encounter on July 29, 2019.

2.3. Satellite-Based and Reanalysis Datasets

High-resolution precipitation data is obtained from the latest NASA Global Precipitation Measurement (GPM) gridded precipitation product, Integrated Multi-SatellitE Retrievals for GPM (IMERG) version 6b algorithm, which fuses early precipitation estimates from the Tropical Rainfall Measuring Mission (Simpson et al., 1988) and the GPM Mission (Huffman, Bolvin, et al., 2015). The multi-satellite precipitation product is available on a 0.1° horizontal grid with global spatial coverage and provides half-hourly and monthly calibrated precipitation estimates for the period June 2000–present (Huffman et al., 2019a, 2019b). The IMERG precipitation products are used throughout the analysis as a means of confirming and comparing suspected

tropical convective events, given that the Saildrone USVs are not outfitted with sensors for measuring in situ rainfall.

Monthly-mean SST fields are obtained from the NOAA Optimum Interpolation Sea Surface Temperature version 2 (OISSTv2) analysis product (Reynolds et al., 2002; Reynolds & Smith, 1995; Smith & Reynolds, 1998). The monthly-mean SST product is based on a linear interpolation of the weekly optimum interpolation (OI) version 2 fields and is available from 1981–present on a 1° horizontal grid with global spatial coverage (https://psl.noaa.gov/data/gridded/data.noaa.oisst.v2.html). In our analysis, we use the NOAA OISSTv2 SST product to assess the mean background field conditions throughout the 2017, 2018, and 2019 Saildrone missions.

The near surface (10-m) wind field, obtained from the ECMWF ERA5 Reanalysis (Hersbach, Bell, Berrisford, Biavati, et al., 2018; Hersbach, Bell, Berrisford, Hirahara, et al., 2020), is shown in the case study presented in Section 4.2. Because the ERA5 hourly mean winds are available on a 0.25° horizontal grid, the entire case study falls within a single gridpoint.

3. Methodology

3.1. Cold Pool Identification

Atmospheric cold pool events sampled by Saildrone USVs are identified as a temperature drop of at least −1.5°C over a 10-min period in raw 1-min mean surface air temperature time series, with the goal of isolating stronger frontal boundaries associated with convective outflow on high-frequency timescales. This air temperature criteria for identifying cold pool fronts is roughly consistent with findings from previous modeling (Feng et al., 2015; Grant et al., 2018; Langhans & Romps, 2015; Tompkins, 2001; Torri et al., 2015) and observational (Chandra et al., 2018; de Szoeke et al., 2017; Garg et al., 2020; Kilpatrick & Xie, 2015; Terai & Wood, 2013) studies of cold pools over the tropical oceans that report average temperature depressions ranging from 1°C to 2°C over an hour or less. For consistency, our cold pool analyses are based on 5-min resolution surface air temperature data available throughout all three missions. Centered differencing is applied to 10-min time windows evaluated every 5 min to identify rapid drops in air temperature. If the threshold is met within a 60-min period for an individual drone, only the first drop is considered to avoid erroneously double-counting events. It should be noted that such instances could reflect collisions between multiple cold pools (Feng et al., 2015; Terai & Wood, 2013), but this is a topic for future research.

3.2. Compositing Scheme

Composite time series analysis is applied to the Saildrone data to evaluate cold pool events, where the beginning of an air temperature drop is defined to start at lag-0, and negative (positive) lags indicate time before (after) a cold pool front passes over the Saildrone USV location. Time-relative anomalies are calculated at each 5-min time step as departures from the −2 h mean lagged field, or the average local environmental conditions over a 120-min period preceding a cold pool front. Ensemble means are generated to evaluate the most robust characteristics of variables (i.e., surface air temperature, specific humidity, wind speed and direction, sea level pressure, and SST and salinity) associated with cold pool events.

4. Results

4.1. Cold Pools Sampled Along Saildrone USV Tracks

The locations of all cold pool events sampled during the three Saildrone missions are shown in Figure 1a. Of the 382 cold pool observations, the majority of events occurred within the ITCZ, or the high precipitation band situated between 6°N and 12°N. While the Saildrone USVs collectively observed 382 cold pools, the actual number of "events" meeting the criteria throughout the study region is less since the USVs likely sampled identical cold pools when in close proximity to each other. All cold pool observations are used in the composite analysis shown in Section 4.3, but the degrees of freedom in the standard error estimates are based on 321 independent events.

The preferential location within the ITCZ is consistent with the relationship between atmospheric cold pools and precipitating downdrafts associated with tropical convection. Similar results were found by Garg et al. (2020), who identified cold pool gust fronts using remotely sensed ocean vector winds from long-term satellite records. In their study, the authors discovered that the spatial distribution of cold pool number density matched well with satellite precipitation climatologies, where the Pacific Ocean ITCZ collocates with the highest number of gust front observations over the ocean. While the frequency of gust fronts is higher over the western Pacific, it was found that the sizes of gust fronts (and thus cold pools) are larger in the central and eastern Pacific, suggesting the influence of organized precipitation due to tropical wave activity in the eastern part of the basin. Our results, which are based on high-frequency variations in surface air temperature derived from in situ observations, further validate the findings of Garg et al. (2020) regarding the linkages between cold pool activity and high-precipitation regimes over the tropical Pacific Ocean.

The magnified maps in Figures 1b–1d depict the Saildrone USV tracks and observed cold pool locations for the individual 2017 (Figure 1d), 2018 (Figure 1c), and 2019 (Figure 1b) Missions, in which La Niña, weak El Niño, and neutral conditions were present, respectively. The results in the bottom row of Figure 1 not only highlight the density of cold pools located within the respective ITCZ regions, but also reveal a handful of cold pools from the 2018 (Figure 1c) and 2019 (Figure 1b) Missions located within 2° of (and on) the equator, where precipitation is sparse due to environmentally stable conditions associated with the seasonal march of the eastern equatorial Pacific Cold Tongue. Given that weak and neutral El Niño conditions were present during these missions, the results likely reflect increased convective activity due to seasonally warmer SSTs along the Equator near 140°W. In contrast, colder SSTs associated with both La Niña and stronger Cold Tongue conditions in the eastern part of the basin during the 2017 Mission (Figure 1d) likely contributed to the lack of cold pool activity observed within the equatorial band near 125°W. Additional cold pools were also observed at higher latitudes within the central and eastern tropical Pacific as the Saildrone USVs traversed to and from the northern launch sites. The number of cold pool observations varies between missions, with approximately 68, 147, and 167 captured in 2017, 2018, and 2019, respectively.

4.2. 2019 Saildrone Mission: Cold Pool Case Study

Saildrone USVs offer the advantage of capturing finer spatial scales of variability when in close proximity to each other, such as the case on July 29, 2019, when four Saildrone USVs encountered the same atmospheric cold pool event near the 2°N, 140°W TAO buoy. Figure 2a highlights the Saildrone USV and TAO mooring positions between 09:00 and 11:00 UTC on July 29, 2019, with the corresponding time series of air temperature and wind speed shown in Figures 2b and 2c. While the TAO data are only available on 10-min intervals, for the 2019 Mission, Saildrone USVs sampled 1-min mean measurements every minute. Despite the differences in data resolution, the results indicate good agreement in air temperature and wind speed observations between the TAO buoy (T) and the closest Saildrone (C), separated by a distance of ∼4 km. The combination of high temporal and spatial resolution Saildrone data (as well as the TAO buoy data) allows us to generate a picture of the atmospheric cold pool evolution as it propagates in space and time. The following timeline (in UTC standard, with 9 UTC being around midnight local time) is presented in tandem with Figure 2:

09:33 Air temperature begins to drop at point A, the southernmost Saildrone. Peak wind speed is recorded 3 min later.

09:38 Air temperature begins to drop at Point B (∼3.7 km northwest of Point A). Peak wind speed is recorded 4 min later.

09:47 Air temperature begins to drop at Point C (∼6.7 km north-northwest of Point B). Peak wind speed is recorded 1 min later.

09:50 Air temperature begins to drop at Point T (∼9 km northwest of Point B). Peak wind speed is recorded simultaneously.

09:53 Air temperature begins to drop at Point D, (∼7.8 km north-northwest of point C). Peak wind speed is recorded 4 min later.

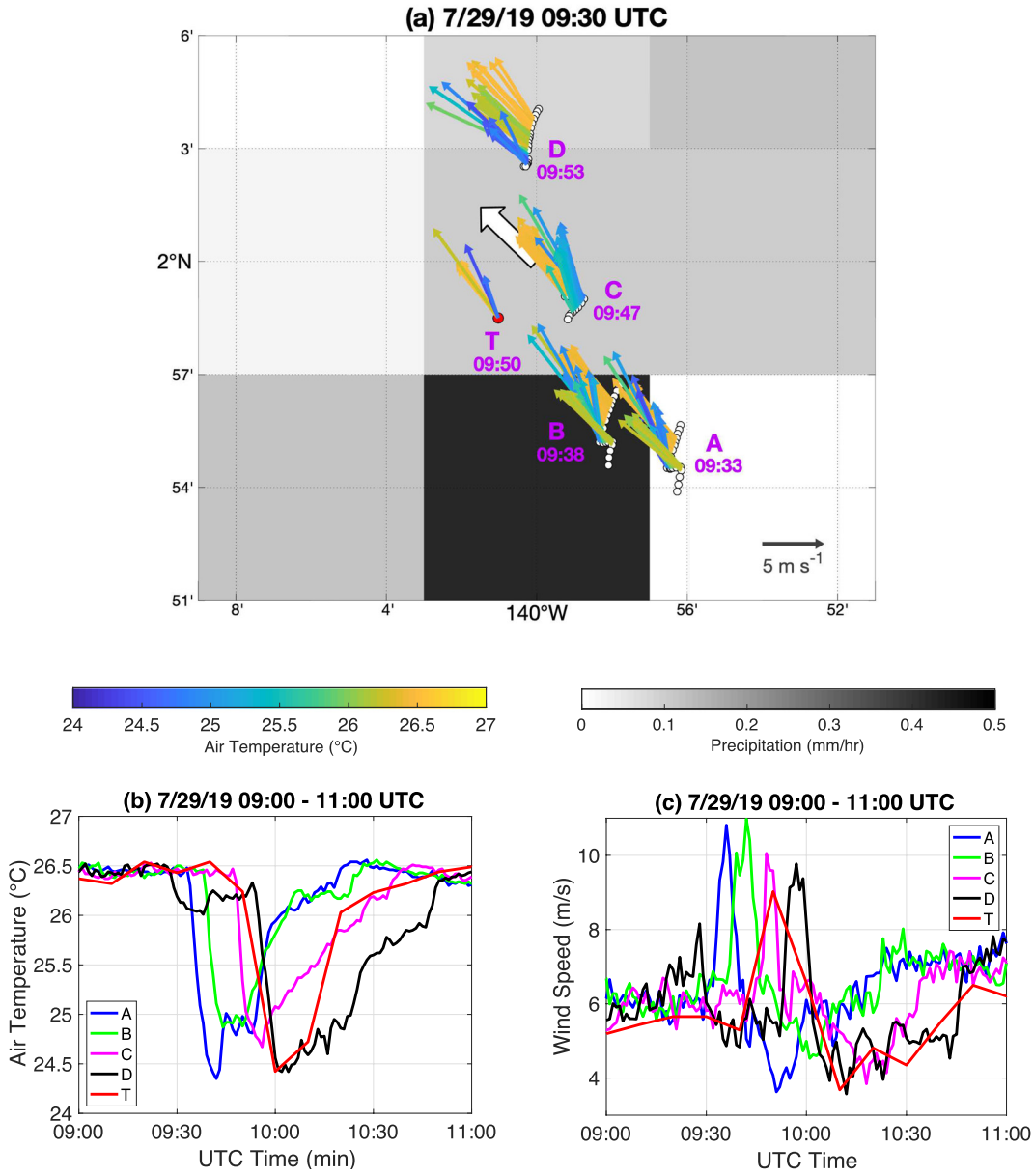

Figure 2. 2019 Mission cold pool event identified on July 29, 2019. (a) Map of four Saildrone USV tracks (white circular markers), the 2°N, 140°W TAO buoy (red circular marker), and wind speed and direction (vectors) over the period 09:00–11:00 UTC on July 29, 2019. Saildrone wind vectors are shaded as a function of air temperature (°C), while hourly 10-m ERA5 winds valid July 29, 2019, 09:00 UTC are depicted by the thick white vector. Satellite precipitation estimates (mm/h; gray shading) valid July 29, 2019, 09:30 UTC are plotted in the background. Saildrone USVs and the TAO buoy are labeled (purple text) A–D and T, respectively, and timestamps indicate the beginning of the air temperature drop at each location. (b and c) Time series of 1-min mean air temperature (b) and wind speed (c) for each of the four Saildrone USVs over the period 09:00–11:00 UTC. Time series are also shown for the TAO buoy (T; red line) available at a resolution of 10 min. For reference, the time series are color coded based on the map labels in the top panel for easier comparison.

Given the timing and location of cold pool interceptions between platforms, we can estimate the direction and propagation speed of the cold pool front at various points throughout its evolution. Prior to encountering the cold pool front, the drones recorded southeasterly winds in agreement with 10-m ERA5 winds (Figure 2a, thick white vector) valid 0900 UTC. The front appears to propagate from the south-southeast to the north-northwest, consistent with the shifts in wind direction at Points A–D and T (Figure 2a, blue-shaded

vectors). The southernmost (Point A) and northernmost (Point D) drones are separated by a distance of approximately 17.1 km and encounter the cold pool within a 20-min period, resulting in an estimated propagation speed of 14.25 m/s across the region. This estimate is close to the estimated propagation speed of ~12.5 m/s for transects A → B, B → C, and B → T; however, the results diverge for transect C → D, with an estimated propagation speed of 21.67 m/s between these two platforms. The estimates assume a normal orientation of the cold pool edge relative to each transect, which is likely not applicable between all platforms.

The propagation speed between platforms would be different if it was estimated based upon the wind speed results in Figure 2c. Background wind speeds around 6 m/s are recorded prior to the event, with winds increasing by 3–5 m/s during the gust front, or period of enhanced wind speeds, behind the cold pool leading edge. The estimated propagation speeds of 12–14 m/s are in better agreement with the numerical findings of Grant et al. (2018), who argue that higher-order gravity waves, with phase speeds around 15 m/s, are more important for modulating the behavior of linear tropical oceanic convective systems. Indeed, while neither the Saildrones nor the TAO mooring collected in situ rainfall measurements, satellite precipitation estimates (i.e., gray shading) valid July 29, 2019, 09:30 UTC in Figure 2a indicate that convection was present over the region, with general system movement from the southeast to the northwest (not shown). However, without the ability to validate results against in situ rainfall observations, it remains unclear to what degree the remotely sensed precipitation measurements are accurate.

The time series in Figures 2b and 2c further confirm the timing of the gust front relative to the timing of the air temperature front at each platform. Generally, wind speeds increase immediately after the temperature drops, as evident from the logical order in which 1-min mean wind speed and air temperature changes across observing platforms. Peak wind speeds recorded by the Saildrones are almost double the pre-frontal conditions and occur within 5 min of encountering the cold pool boundary, with gust fronts lasting for a period of approximately 10 min. In comparison, the 10-min resolution TAO time series indicate that the beginning of the air temperature front coincides with the timing of peak wind speeds. The apparent lower and longer peak winds at the TAO buoy, in comparison to those recorded by Saildrone USVs, are likely associated with differences in the temporal resolution, which is lower for TAO (10 min) than for USV in this case study (1 min).

4.3. Cold Pool Composite Time Series

The timing of the wind gust relative to the temperature drop becomes more clear when we consider the composite time series over all atmospheric cold pool events observed by the USVs. As described in Section 3.1, cold pool events are identified by an air temperature drop of at least −1.5°C over 10 min. The results in Figure 3 show the ensemble-mean composite time series of oceanic and meteorological variables associated with the 382 cold pool observations captured by Saildrone USVs from the 2017, 2018, and 2019 missions combined. Unlike the time series shown in Figure 2, the composite time series in Figure 3 are plotted on 5-min intervals for consistency due to different sensor sampling schemes between missions. Anomalies are calculated at each time step relative to the -2 h mean field, but composite values are only shown for the 60 min period leading and 120 min period lagging the atmospheric cold pool front. For compositing purposes, we treat each Saildrone USV measurement as an independent observation given the different spatial and temporal vantage points each drone provides, but the standard error of the ensemble-mean at each time step (e.g., blue error bars) is adjusted to account for "duplicate" events in which two or more drones observe a cold pool less than 60 min apart within a distance of 100 km.

The ensemble-mean air temperature composite in Figure 3a indicates that air temperature anomalies trend closer to zero at negative lags compared to positive lags. While the Saildrone USVs are moving platforms, their positions are considered mostly stationary relative to the scale of a frontal passage, only moving an average distance of 0.4 and 0.75 km (in 5 and 10 min, respectively) away from their previous position (not shown). Hence, we view each cold pool event as a front that passes the USV, where air temperature observations prior to the front (i.e., negative lags) are considered to reflect ambient conditions, and observations following the front (i.e., positive lags) are considered to reflect the local anomalous air temperature field within a cold pool.

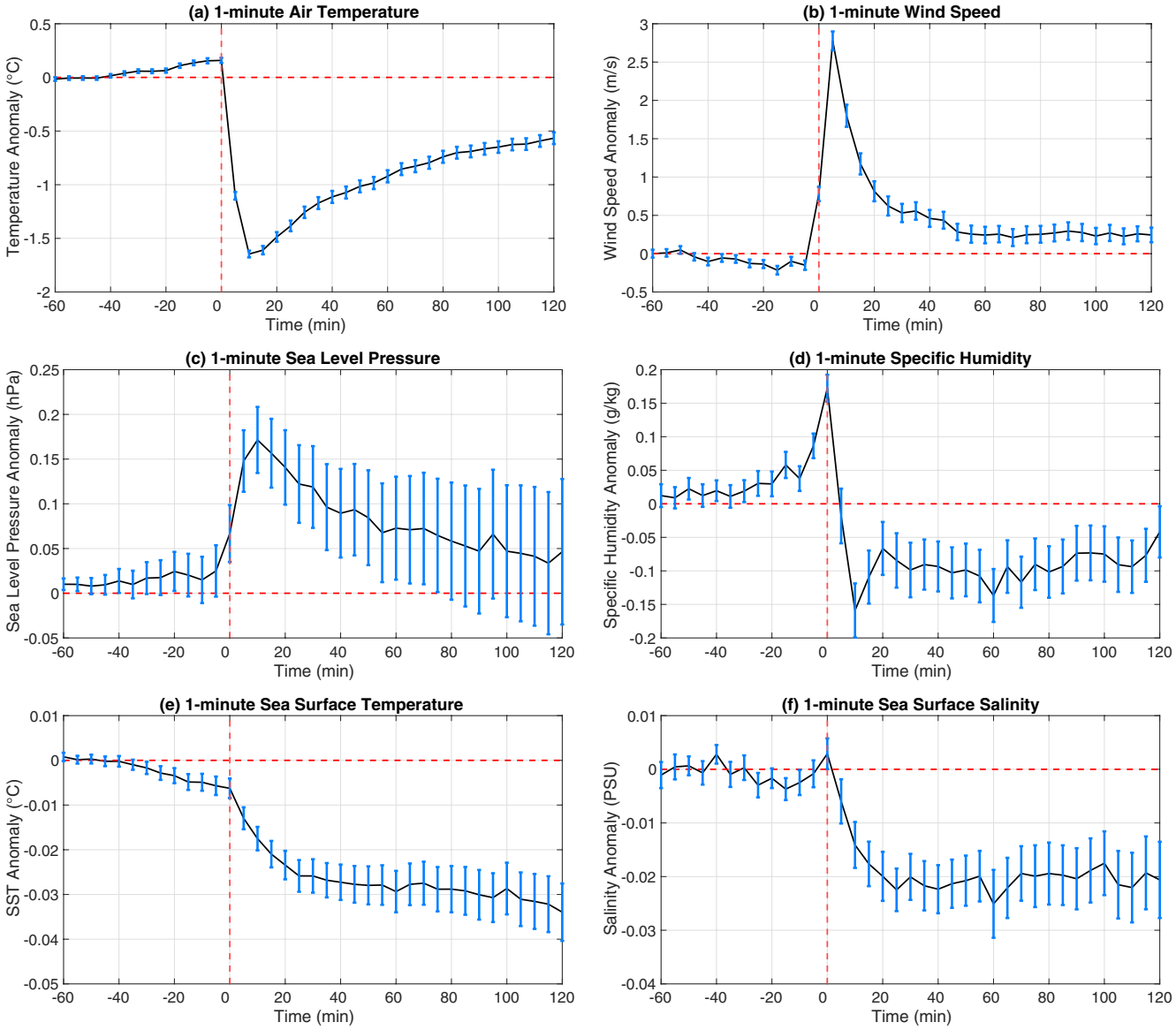

Figure 3. Ensemble-mean composites of 1-min mean air temperature (°C; a), wind speed (m/s; b), sea level pressure (hPa; c), specific humidity (g/kg; d), SST (°C; e), and sea surface salinity (PSU; f) associated with cold pool events sampled by Saildrone USVs across all three missions. Error bars are shown in blue and denote the standard error of the ensemble mean at each time step based on 321 degrees of freedom. Anomalies are calculated relative to the −2 h mean field, and negative (positive) lags indicate the anomalous fields before (after) a cold pool front, defined to begin at lag-0.

The air temperature results in Figure 3a reveal two key features associated with atmospheric cold pools. First, there is a clear decrease in air temperature following the beginning of the cold pool front (defined to begin at lag-0). This robust rapid decrease, with a mean feature of −1.8°C/10 min, is expected based on the cold pool identification criteria described in Section 3.1. It is interesting to note that the most rapid temperature change occurs between lags of 0 and +5 min, with a mean temperature drop of −1.3°C, indicating a stronger frontal boundary along the cold pool edge. The rapid drop in air temperature is broadly consistent with results found in similar observational studies (Chandra et al., 2018; de Szoeke et al., 2017), though the mean 10-min frontal period observed by Saildrone USVs appears shorter than the mean ∼20 min frontal period reported in the studies. While the shorter frontal period is likely a product of the detection method, the criteria does not constrain the temperature depression to reach its minimum by the end of the 10-min window.

The second key feature is the asymmetry of air temperature anomalies preceding (i.e., negative lags) and following (i.e., positive lags) the cold pool front in Figure 3. The asymmetry in the air temperature field reflects the slower recovery of the atmosphere to background environmental conditions within the cold pool at positive lags. This is consistent with results from previous observational and modeling studies that reported average recovery timescales ranging from 20 min to 3 h or longer depending on the type of cold pool (i.e., isolated vs. intersecting) sampled (Chandra et al., 2018; de Szoeke et al., 2017; Feng et al., 2015; Kilpatrick & Xie, 2015; Tompkins, 2001; Zuidema et al., 2017). The results indicate a mean air temperature recovery of 1°C over a 2 h period following the frontal passage, but it is difficult to assess recovery statistics from Saildrone observations alone, given that the drones are continuously moving, the position of the Saildrone relative to the center of the sampled cold pool is unknown, and the diurnal cycle may influence the composite results.

In addition to air temperature, the ensemble-mean wind speed result in Figure 3b is robust and reveals a slight increase in 1-min mean wind speed (up to 1 m/s) immediately preceding and coincident with the decrease in air temperature (e.g., Figure 3a). Importantly, wind speed anomalies peak up to 3 m/s in the 5-min period following the initial frontal passage, marking an almost 50% increase in wind speed compared to the mean background wind speed of ∼6.6 m/s in the hour before encountering a cold pool. The latter result reflects the "gust front" associated with the leading edge of the cold air mass and is consistent with previous findings that suggest the strongest winds trail behind the cold pool's leading edge (Charba, 1974; Grant & van den Heever, 2016). In fact, Saildrone observations reveal 1-min mean wind speed anomalies peaking as high as 10 m/s during individual cold pool gust fronts (not shown). The apparent relationship between strong gradients in air temperature and horizontal winds associated with cold pools further validates the results of Garg et al. (2020) who use satellite retrievals to identify cold pool signatures in the horizontal wind field.

Concurrent with the gust front, the ensemble-mean sea level pressure (SLP) anomalies in Figure 3c indicate positive, albeit small, SLP perturbations up to 0.17 hPa, slightly increasing at the beginning of the front. Interestingly, the ensemble-mean specific humidity time series in Figure 3d indicate a positive anomaly of 0.17 g/kg coincident with the cold pool edge at lag-0 and a negative anomaly of −0.16 g/kg coincident with the air temperature minimum at a lag of +10 min. The decrease in specific humidity following the frontal passage is consistent with the advection of drier, colder air from inside the cold pool, while the increase in specific humidity prior to the cold pool front, in conjunction with increased surface pressure, is suggestive of wind and moisture convergence and is consistent with findings documented in previous observational studies (Chandra et al., 2018; de Szoeke et al., 2017).

Figures 3e and 3f highlight the composite time series results for sea surface temperature (SST) and sea surface salinity (SSS), respectively. Compared to the atmospheric fields, the oceanic fields appear to change gradually following the passage of the cold pool front, with SST and SSS decreasing by −0.025°C and −0.025 PSU in 25 min, respectively. The relatively small changes in the SST field have important implications for the calculation of surface sensible heat fluxes, as rapidly decreasing air temperature will act to increase the air-sea temperature difference during cold pool events. The SST and SSS anomalies also persist longer than a lag of +120 min, suggestive of the formation of a cooler, fresh water lens associated with the parent tropical convection (Pei et al., 2018). However, without the verification of in situ rainfall measurements and ship-borne radar, it is unknown where the Saildrones are located relative to the parent convection and if they encounter precipitation along their tracks.

5. Conclusions

High-resolution, in situ observations collected by Saildrone USV are used to investigate high-frequency variations in surface meteorological variables associated with atmospheric cold pools during three missions to previously unexplored, remote regions of the central and eastern (∼140°W–125°W) tropical Pacific Ocean. Atmospheric cold pools are identified based on raw 1-min mean time series of surface air temperature, where rapid temperature variations meeting a threshold criteria of −1.5°C/10 min are considered. Ensemble-mean composite time series based on 382 cold pool observations (321 independent cold pool events) from 10 total Saildrones reveal the following:

1. Cold pools meeting the minimum criteria exhibit a mean temperature drop of −1.8°C/10 min, but the temperature change is most rapid along the leading edge of the cold pool boundary, with an initial air temperature front of −1.3°C/5 min
2. The air temperature drop is associated with increased winds and immediately followed by the gust front, or a period of enhanced wind speeds. Peak 1-min mean wind speeds up to 3 m/s occur within 5 min of the air temperature drop, indicating an almost 50% increase in wind speed compared to mean pre-frontal conditions
3. Positive anomalies in SLP and specific humidity of 0.17 hPa and 0.17 g/kg, respectively, coincide with the beginning of the air temperature drop, suggestive of wind and moisture convergence along the cold pool boundary. A negative specific humidity anomaly of −0.16 g/kg coincides with the air temperature minimum 10 min later, consistent with the advection of drier, colder air from inside the cold pool
4. SST and SSS decrease by −0.025°C and −0.025 PSU, respectively, over the 25-min period following the cold pool front. The induced cooler and fresher lenses in the ocean last much longer than the atmospheric cold pools

In addition to the composite results, a cold pool case study is presented for four Saildrone USVs that encountered the same event near the TAO buoy at 2°N, 140°W during the 2019 Mission. The combination of platforms provided unique temporal and spatial vantage points, acting as a traveling "mesoscale network" (Brock et al., 1995; Engerer et al., 2008) of in situ observing platforms that resolves information on the propagation speed, strength, and position of the atmospheric cold pool front as it evolved over the ocean. Satellite precipitation estimates indicated rainfall along the cold pool boundary, but the results could not be validated in the absence of in situ rain measurements (including at the TAO buoy). Nevertheless, the increased areal coverage due to multiple Saildrone platforms, in concert with the TAO buoy observations, satellite precipitation estimates, and reanalysis winds allows for a comprehensive analysis of small-scale phenomena over observationally spare ocean regions.

While we focused on key state variables throughout this study, the application of Saildrone USV data is expansive. Future analyses will focus on high-frequency variations in wind speeds and the implications for calculating gustiness parameters in bulk algorithms to resolve air-sea heat fluxes during cold pool gust fronts. Additional analyses will focus on resolving the diurnal cycle of atmospheric cold pools over the central and eastern tropical Pacific, and Saildrone observations will be analyzed in the context of historical TAO buoy records over the ocean.

Data Availability Statement

Saildrone data used in this study are provided by NOAA/PMEL Ocean Climate Stations and available for download at https://www.pmel.noaa.gov/ocs/saildrone/data-access. TAO data used in this study are provided by the GTMBA Project Office of NOAA/PMEL and available for download at https://www.pmel.noaa.gov/tao/drupal/disdel/. NOAA OISST V2 data used in this study were provided by the NOAA/OAR/ESRL PSL Boulder, Colorado, USA, from their website at https://psl.noaa.gov/data/gridded/data.noaa.oisst.v2.html. The GPM IMERG data used in this study were provided by the NASA/Goddard Space Flight Center's Precipitation Measuring Mission and Precipitation Processing System and available at https://doi.org/10.5067/GPM/IMERG/3B-HH/06 and https://doi.org/10.5067/GPM/IMERG/3B-MONTH/06. The ERA5 global reanalysis data used is this study were generated using Copernicus Climate Change Service information 2021 and available for download at https://doi.org/10.24381/cds.adbb2d47.

Acknowledgments
The authors thank the two anonymous reviewers who provided insightful comments to improve the first version of the manuscript. They thank Saildrone, Inc. for their piloting and engineering efforts and for providing additional seadays during the 2017, 2018, and 2019 Saildrone Missions. This work was supported by NOAA's Global Ocean Monitoring and Observing Program, NOAA's Climate Program Office/Climate Variability and Predictability Program, and NOAA's Office of Marine and Aviation Operations. This publication is PMEL contribution 5221 and CICOES contribution 2020-1136.

References

Betts, A. K., Dias, M. F. S. (1979). Unsaturated downdraft thermodynamics in cumulonimbus. *Journal of the Atmospheric Sciences*, *36*(6), 1061–1071. https://doi.org/10.1175/1520-0469(1979)036⟨1061:UDTIC⟩2.0.CO;2

Brock, F. V., Crawford, K. C., Elliott, R. L., Cuperus, G. W., Stadler, S. J., Johnson, H. L., & Eilts, M. D. (1995). The Oklahoma mesonet: A technical overview. *Journal of Atmospheric and Oceanic Technology*, *12*(1), 5–19. https://doi.org/10.1175/1520-0426(1995)012⟨0005:TOMATO⟩2.0.CO;2

Chandra, A. S., Zuidema, P., Krueger, S., Kochanski, A., de Szoeke, S. P., & Zhang, J. (2018). Moisture distributions in tropical cold pools from equatorial Indian Ocean observations and cloud-resolving simulations. *Journal of Geophysical Research-D: Atmospheres*, *123*(20), 445–511. https://doi.org/10.1029/2018JD028634

Charba, J. (1974). Application of gravity current model to analysis of squall-line gust front. *Monthly Weather Review*, *102*(2), 140–156. https://doi.org/10.1175/1520-0493(1974)102⟨0140:AOGCMT⟩2.0.CO;2

Cravatte, S., Kessler, W., Smith, N., Wijffels, S., Yu, L., Ando, K., et al. (2016). *First report of tpos 2020 (Tech. Rep.)*. GOOS-215, 200 pp. Available online at http://tpos2020.org/first-report/

de Szoeke, S. P., Skyllingstad, E. D., Zuidema, P., & Chandra, A. S. (2017). Cold pools and their influence on the tropical marine boundary layer. *Journal of the Atmospheric Sciences*, *74*(4), 1149–1168. https://doi.org/10.1175/JAS-D-16-0264.1

Emanuel, K. A., David Neelin, J., & Bretherton, C. S. (1994). On large-scale circulations in convecting atmospheres. *Quarterly Journal of the Royal Meteorological Society*, *120*(519), 1111–1143. https://doi.org/10.1002/qj.49712051902

Engerer, N. A., Stensrud, D. J., & Coniglio, M. C. (2008). Surface characteristics of observed cold pools. *Monthly Weather Review*, *136*(12), 4839–4849. https://doi.org/10.1175/2008MWR2528.1

Feng, Z., Hagos, S., Rowe, A. K., Burleyson, C. D., Martini, M. N., & Szoeke, S. P. (2015). Mechanisms of convective cloud organization by cold pools over tropical warm ocean during the AMIE/DYNAMO field campaign. *Journal of Advances in Modeling Earth Systems*, *7*(2), 357–381. https://doi.org/10.1002/2014MS000384

Garg, P., Nesbitt, S. W., Lang, T. J., Priftis, G., Chronis, T., Thayer, J. D., & Hence, D. A. (2020). Identifying and characterizing tropical oceanic mesoscale cold pools using spaceborne scatterometer winds. *Journal of Geophysical Research-D: Atmospheres*, *125*(5), e2019JD031812. https://doi.org/10.1029/2019JD031812

Gentine, P., Garelli, A., Park, S. B., Nie, J., Torri, G., & Kuang, Z. (2016). Role of surface heat fluxes underneath cold pools. *Geophysical Research Letters*, *43*(2), 874–883. https://doi.org/10.1002/2015GL067262

Glickman, T. S., & Zenk, W. (2000). *Glossary of meteorology* (2nd ed.). AMS (American Meteorological Society).

Grant, L. D., Lane, T. P., & van den Heever, S. C. (2018). The role of cold pools in tropical oceanic convective systems. *Journal of the Atmospheric Sciences*, *75*(8), 2615–2634. https://doi.org/10.1175/JAS-D-17-0352.1

Grant, L. D., & van den Heever, S. C. (2016). Cold pool dissipation. *Journal of Geophysical Research-D: Atmospheres*, *121*(3), 1138–1155. https://doi.org/10.1002/2015JD023813

Hersbach, H., Bell, B., Berrisford, P., Biavati, G., Horányi, A., Muñoz-Sabater, J., et al. (2018). *Era5 hourly data on single levels from 1979 to present*. Copernicus Climate Change Service (C3S) Climate Data Store (CDS). https://doi.org/10.24381/cds.adbb2d47

Hersbach, H., Bell, B., Berrisford, P., Hirahara, S., Horányi, A., Muñoz-Sabater, J, et al. (2020). The era5 global reanalysis. *Quarterly Journal of the Royal Meteorological Society*, *146*(730), 1999–2049. https://doi.org/10.1002/qj.3803

Huffman, G. J., Bolvin, D. T., Braithwaite, D., Hsu, K., Joyce, R., Xie, P., & Yoo, S.-H. (2015). NASA Global Precipitation Measurement (GPM) Integrated Multi-Satellite Retrievals for GPM (IMERG). *Algorithm Theoretical Basis Document (ATBD) Version*, *4*, 26.

Huffman, G. J., Stocker, E. F., Bolvin, D. T., Nelkin, E. J., & Tan, J. (2019a). *GPM IMERG final precipitation L3 half hourly 0.1 degree x 0.1 degree v06*. Goddard Earth Sciences Data and Information Services Center. https://doi.org/10.5067/GPM/IMERG/3B-HH/06

Huffman, G. J., Stocker, E. F., Bolvin, D. T., Nelkin, E. J., & Tan, J. (2019b). *GPM IMERG final precipitation L3 month 0.1 degree x 0.1 degree v06*. Goddard Earth Sciences Data and Information Services Center. https://doi.org/10.5067/GPM/IMERG/3B-MONTH/06

Kessler, W. S., Wijffels, S. E., Cravatte, S., Smith, N., Kumar, A., Fujii, Y., et al. (2019). *Second report of tpos 2020 (Tech. Rep.)*. GOOS-234. Retrieved from http://tpos2020.org/second-report/

Kilpatrick, T. J., & Xie, S. P. (2015). ASCAT observations of downdrafts from mesoscale convective systems. *Geophysical Research Letters*, *42*(6), 1951–1958. https://doi.org/10.1002/2015GL063025

Lafore, J.-P., & Moncrieff, M. W. (1989). A numerical investigation of the organization and interaction of the convective and stratiform regions of tropical squall lines. *Journal of the Atmospheric Sciences*, *46*(4), 521–544. https://doi.org/10.1175/1520-0469(1989)046⟨0521:ANIOTO⟩2.0.CO;2

Langhans, W., & Romps, D. M. (2015). The origin of water vapor rings in tropical oceanic cold pools. *Geophysical Research Letters*, *42*(18), 7825–7834. https://doi.org/10.1002/2015GL065623

Li, Z., Zuidema, P., & Zhu, P. (2014). Simulated convective invigoration processes at trade wind cumulus cold pool boundaries. *Journal of the Atmospheric Sciences*, *71*(8), 2823–2841. https://doi.org/10.1175/JAS-D-13-0184.1

Lindstrom, E., Shcherbina, A. Y., Shcherbina, A., Rainville, L., Farrar, T., Centurioni, L., et al. (2017). Autonomous multi-platform observations during the salinity processes in the upper-ocean regional study. *Oceanography*, *30*(2), 38–48. https://doi.org/10.5670/oceanog.2017.218

McPhaden, M., Busalacchi, A., & Anderson, D. (2010). A toga retrospective. *Oceanography*, *23*(3), 86–103. https://doi.org/10.5670/oceanog.2010.26

McPhaden, M. J., Busalacchi, A. J., Cheney, R., Donguy, J.-R., Gage, K. S., Halpern, D., et al. (1998). The tropical ocean-global atmosphere observing system: A decade of progress. *Journal of Geophysical Research*, *103*(C7), 14169–14240. https://doi.org/10.1029/97JC02906

Pei, S., Shinoda, T., Soloviev, A., & Lien, R.-C. (2018). Upper ocean response to the atmospheric cold pools associated with the Madden-Julian oscillation. *Geophysical Research Letters*, *45*(10), 5020–5029. https://doi.org/10.1029/2018GL077825

Raymond, D. J., Esbensen, S. K., Paulson, C., Gregg, M., Bretherton, C. S., Petersen, W. A., et al. (2004). EPIC2001 and the coupled ocean-atmosphere system of the tropical east Pacific. *Bulletin of the American Meteorological Society*, *85*(9), 1341–1354. https://doi.org/10.1175/BAMS-85-9-1341

Reynolds, R. W., Rayner, N. A., Smith, T. M., Stokes, D. C., & Wang, W. (2002). An improved in situ and satellite SST analysis for climate. *Journal of Climate*, *15*(13), 1609–1625. https://doi.org/10.1175/1520-0442(2002)015⟨1609:AIISAS⟩2.0.CO;2

Reynolds, R. W., & Smith, T. M. (1995). A high-resolution global sea surface temperature climatology. *Journal of Climate*, *8*(6), 1571–1583. https://doi.org/10.1175/1520-0442(1995)008⟨1571:AHRGSS⟩2.0.CO;2

Ross, A. N., Tompkins, A. M., & Parker, D. J. (2004). Simple models of the role of surface fluxes in convective cold pool evolution. *Journal of the Atmospheric Sciences*, *61*(13), 1582–1595. https://doi.org/10.1175/1520-0469(2004)061⟨1582:SMOTRO⟩2.0.CO;2

Saxen, T. R., & Rutledge, S. A. (1998). Surface fluxes and boundary layer recovery in TOGA COARE: Sensitivity to convective organization. *Journal of the Atmospheric Sciences*, *55*(17), 2763–2781. https://doi.org/10.1175/1520-0469(1998)055⟨2763:SFABLR⟩2.0.CO;2

Serra, Y. L. (2018). Precipitation measurements from the tropical moored array: A review and look ahead. *Quarterly Journal of the Royal Meteorological Society*, *144*, 221–234. https://doi.org/10.1002/qj.3287

Simpson, J., Adler, R. F., & North, G. R. (1988). A proposed tropical rainfall measuring mission (TRMM) satellite. *Bulletin of the American Meteorological Society*, *69*(3), 278–295. https://doi.org/10.1175/1520-0477(1988)069⟨0278:APTRMM⟩2.0.CO;2

Skyllingstad, E. D., & de Szoeke, S. P. (2015). Cloud-resolving large-eddy simulation of tropical convective development and surface fluxes. *Monthly Weather Review*, *143*(7), 2441–2458. https://doi.org/10.1175/MWR-D-14-00247.1

Smith, T. M., & Reynolds, R. W. (1998). A high-resolution global sea surface temperature climatology for the 1961–90 base period. *Journal of Climate*, *11*(12), 3320–3323. https://doi.org/10.1175/1520-0442(1998)011⟨3320:AHRGSS⟩2.0.CO;2

Terai, C. R., & Wood, R. (2013). Aircraft observations of cold pools under marine stratocumulus. *Atmospheric Chemistry and Physics*, *13*(19), 9899–9914. https://doi.org/10.5194/acp-13-9899-2013

Tompkins, A. M. (2001). Organization of tropical convection in low vertical wind shears: The role of cold pools. *Journal of the Atmospheric Sciences*, *58*(13), 1650–1672. https://doi.org/10.1175/1520-0469(2001)058⟨1650:OOTCIL⟩2.0.CO;2

Torri, G., Kuang, Z., & Tian, Y. (2015). Mechanisms for convection triggering by cold pools. *Geophysical Research Letters*, *42*(6), 1943–1950. https://doi.org/10.1002/2015GL063227

Young, G. S., Perugini, S. M., & Fairall, C. W. (1995). Convective wakes in the equatorial western pacific during TOGA. *Monthly Weather Review*, *123*(1), 110–123. https://doi.org/10.1175/1520-0493(1995)123⟨0110:CWITEW⟩2.0.CO;2

Yuter, S. E., & Houze, R. A., Jr (2000). The 1997 Pan American climate studies tropical eastern Pacific process study. Part I: ITCZ Region. *Bulletin of the American Meteorological Society*, *81*(3), 451–481. https://doi.org/10.1175/1520-0477(2000)081⟨0451:TPACST⟩2.3.CO;2

Zhang, D., Cronin, M. F., Cronin, M., Meing, C., Farrar, J. T., Jenkins, R., et al. (2019). Comparing air-sea flux measurements from a new unmanned surface vehicle and proven platforms during the spurs-2 field campaign. *Oceanography*, *32*(2), 122–133. https://doi.org/10.5670/oceanog.2019.220

Zuidema, P., Torri, G., Muller, C., & Chandra, A. (2017). A survey of precipitation-induced atmospheric cold pools over oceans and their interactions with the larger-scale environment. *Surveys in Geophysics*, *38*(6), 1283–1305. https://doi.org/10.1007/s10712-017-9447-x